Highly Conductive Quasi-1D Hexagonal Chalcogenide Perovskite $Sr_8Ti_7S_{21}$ with Efficient Polysulfide Regulation in Lithium-Sulfur Batteries

Dawei Yang[+,], Yanbing Han[+], Mengyao Li, Canhuang Li, Wei Bi, Qianhong Gong, Jinglu Zhang, Han Gao, Jordi Arbiol, Zhifeng Shi*, Guangmin Zhou*, Andreu Cabot**

Dr. D. W. Yang, W. Bi, Q. H. Gong
Henan Province Key Laboratory of Photovoltaic Materials, School of Future Technology, Henan University, Kaifeng, 475004, P. R. China
Email: dwyang@henu.edu.cn

Dr. Y. B. Han, Dr. M. Y. Li, J. L. Zhang, Dr. H. Gao, Prof. Z. F. Shi
Key Laboratory of Materials Physics of Ministry of Education, School of Physics and Microelectronics, Zhengzhou University, Daxue Road 75, Zhengzhou, 450052 China
Email: shizf@zzu.edu.cn

Prof. J. Arbiol
Catalan Institute of Nanoscience and Nanotechnology (ICN2), Campus UAB, Bellaterra, 08193 Barcelona, Catalonia, Spain

Prof. G. M. Zhou
Tsinghua-Berkeley Shenzhen Institute & Tsinghua Shenzhen International Graduate School, Tsinghua University, Shenzhen, 518055 P. R. China
Email: guangminzhou@sz.tsinghua.edu.cn

Dr. C. H. Li, Prof. A. Cabot
Catalonia Institute for Energy Research - IREC
Sant Adrià de Besòs, Barcelona, 08930, Spain
Email: acabot@irec.cat

Prof. J. Arbiol, Prof. A. Cabot
ICREA
Pg. Lluís Companys 23, 08010 Barcelona, Spain

+ These authors contributed equally to this work

Abstract

Lithium-sulfur batteries (LSBs) are considered among the most promising candidates for next-generation energy storage systems. However, the commercialization of LSBs faces various technical challenges, sucs as the notorious migration of polysulfide from the cathode to the anode and sluggish sulfur conversion kinetics. In this context, we present a quasi-1D hexagonal chalcogenide perovskite, $Sr_8Ti_7S_{21}$, as an efficient sulfur host capable of overcoming these limitations. Both experimental results and density functional theory calculations demonstrate that $Sr_8Ti_7S_{21}$ exhibits robust binding with lithium polysulfides through through the formation of multiple bonds. Additionally, $Sr_8Ti_7S_{21}$ effectively enhances the kinetics of the LiPS redox reaction. Consequently, cathodes based on $S@Sr_8Ti_7S_{21}$ demonstrate outstanding initial capacities up to 1315 mAh g^{-1} at 0.2C, remarkable cycling stability with an average capacity decay rate of 0.08% per cycle over 400 cycles at 1C, and a high areal capacity of 6.58 mAh cm^{-2} under a substantial sulfur loading of 6.5 mg cm^{-2}. This study highlights the potential capabilities and promising prospects of chalcogenide perovskites in advancing LSBs technology.

Keywords: Quasi-1D chalcogenide perovskite, $Sr_8Ti_7S_{21}$, lithium polysulfides, catalytic conversion, lithium-sulfur batteries

1. Introduction

Lithium-sulfur batteries (LSBs) have received extensive attention associated with their high potential theoretical capacity (1672 mAh g^{-1}), energy density (2600 Wh kg^{-1}), cost-effectiveness, and sulfur abundance.[1] However, their commercial deployment is still hampered by several unsolved drawbacks, such as: i) the electrically insulating nature of sulfur and Li_2S/Li_2S_2;[2] ii) the migration of the soluble intermediate lithium polysulfides (LiPS);[3] and iii) a slow conversion kinetics of the complex Li-S redox reactions that involve numerous electrons and a liquid/solid phase transition.[4] These drawbacks result in low utilization of the active material and a rapid decline in battery capacity, especially at the high loadings required for LSB industrialization.

Several strategies have been proposed to address these limitations. One effective approach to increase the cathode electrical conductivity and confine the LiPS is to combine sulfur with conductive porous carbons.[3b, 5] However, nonpolar carbon offers weak physisorption of polar LiPS, which prevents efficient LiPS trapping. The addition of metal-based compounds has shown improved effectiveness in confining LiPS.[6] Nevertheless, chemical adsorption alone is insufficient to fully address the above limitations since adsorption sites become rapidly saturated if no active catalytic effect is anticipated to overcome the slow LiPS reaction kinetics. In this direction, the incorporation of electrocatalytic materials that interact with LiPS and can significantly reduce the energy barrier for their conversion has become essential in the development of the new LSB generations.[7]

Chalcogenide perovskites are generally characterized by excellent charge transport properties,[8] high light absorption,[9] and a high tolerance to defects.[10] These properties have provided them with great momentum in the field of catalysis. $BaZrS_3$ is a representative chalcogenide perovskite with a distorted structure.[11] Within $BaZrS_3$, Zr-S_6 octahedra connect each other in a 3D orthorhombic network via corner-sharing, providing moderately anisotropic properties. On the other hand, within hexagonal chalcogenide perovskites like $BaTiS_3$, Ti-S_6 octahedra are connected in a 1D chain via face-sharing, leading to large property anisotropies.[12]

Here, we propose the use of hexagonal chalcogenide perovskites like $Sr_8Ti_7S_{21}$ as a sulfur host in LSBs. $Sr_8Ti_7S_{21}$ is characterized by a relatively narrow band gap (0.97 eV), excellent electrical conductivity, and high electrochemical stability.[13] In the crystal structure of $Sr_8Ti_7S_{21}$,

the Ti-S_6 octahedra connect each other by sharing triangular facets, forming 1D chains. These 1D Ti-S_6 chains are separated by Sr cations. Therefore, $Sr_8Ti_7S_{21}$ is considered to exhibit a quasi-1D structure. Besides, the chemical bonding between the inter-chains is weaker than that along the intra-chain direction, similar to the case of 2D materials MoS_2.[14] This fact may lead to a higher Li ion transport efficiency in the paths along the 1D Ti-S_6 chains within the $Sr_8Ti_7S_{21}$ structure. Additionally, $Sr_8Ti_7S_{21}$ contains numerous intrinsic defects due to its off-stoichiometry which can serve as active centers for adsorption and catalysis. Last but not least, Sr and Ti are relatively abundant metals in the Earth's crust,[15] which overall makes $Sr_8Ti_7S_{21}$ a sustainable candidate material as S host in LSBs. However, despite all these advantages, its performance is yet to be explored.

In this work, the $Sr_8Ti_7S_{21}$ perovskite is explored as a cathode additive to immobilize LiPS and guide Li_2S deposition in a working LSB. We determine its LiPS adsorption capability and activity towards the Li-S redox reactions. Besides, the performance of S@$Sr_8Ti_7S_{21}$ cathodes is thoroughly tested to demonstrate their superior cycling stability and rate capability. The obtained results are finally rationalized with the help of density functional theory (DFT) calculations.

2. Results and discussions

The $Sr_8Ti_7S_{21}$ powder was was synthesized using the same method employed previously for the preparation of $BaZrS_3$[11] and $SrZrS_3$[8] (**Figure 1a,** see details in the supporting information, SI). Briefly, a commercial $SrTiO_3$ powder underwent grinding and sieving to eliminate large particles that could impede sulfurization. The SEM images in Figure S1, demonstrate the uniform particle sizes of the processed $SrTiO_3$ powder. Subsequently, the $SrTiO_3$ powder was placed in a quartz boat within a tube furnace. Prior to sulfurization, the tube furnace was pumped down below 0.1 Pa. Sulfurization took place at 1000 ºC for 120 minutes, using CS_2 as the sulfur source. Following sulfurization, the tube furnace was cooled to room temperature, an the resulting $Sr_8Ti_7S_{21}$ powder was collected (Figure S2). The $Sr_8Ti_7S_{21}$ grains exhibited a larger size than $SrTiO_3$ grains, indicating some degree of crystal growth/aglomeration during the high-temperature sulfurization process.

X-ray diffraction (XRD) analysis of the final product (Figure 1b) confirmed its crystal structure to match that of $Sr_8Ti_7S_{21}$. To elucidate the formation of $Sr_8Ti_7S_{21}$ instead of $SrTiS_3$, energy dispersive X-ray spectroscopy (EDX) analysis was employed to analyze the material's composition (Figure 1d). After normalizing the Sr peak, the Ti signal exhibited a significant 10% decrease in intensity when transitioning from $SrTiO_3$ to $Sr_8Ti_7S_{21}$. Using commercial $SrTiO_3$ as a reference with a Sr/Ti ratio of exactly 1, the Sr:Ti:S ratio was determined as 1:0.91:2.65, confirming the composition of the final powder as $Sr_8Ti_7S_{21}$. EDS mapping in Figure 1c indicated the uniform distribution of the constituent elements.

The TEM images of perovskite $Sr_8Ti_7S_{21}$ are presented in Figure 1e and Figure S3, revealing lattice fringes with a pitch of 2.6 Å, corresponding to the (008) plane family of perovskite $Sr_8Ti_7S_{21}$. Figure 1f,g depict the crystal structure and a high-resolution transmission electron microscopy (HRTEM) image of $Sr_8Ti_7S_{21}$ powder. The near-parallel Sr lines form hexagons, as highlighted in red, with face-sharing Ti-S_6 octahedra in the center. The distance between two opposite vertices measures 8 Å from the HRTEM image, consistent with the $Sr_8Ti_7S_{21}$ crystal structure (7.9 Å).

X-ray photoelectron spectroscopy (XPS) analysis reveals that the Sr 3d spectra align with an Sr^{2+} chemical environment, with minimal shifts observed when transitioning from $SrTiO_3$ to $Sr_8Ti_7S_{21}$ (Figure 1h).[16] In the Ti $2p_{3/2}$ spectrum of $SrTiO_3$, a solitary peak at 458.2 eV indicates

a Ti^{4+} valence state, as anticipated (Figure 1i). However, the Ti $2p_{3/2}$ XPS spectrum of $Sr_8Ti_7S_{21}$ exhibits two discernible contributions labeled as Ti-A (457.9 eV) and Ti-B (455.6 eV), where Ti-A corresponds to a +4 valence state, and Ti-B (the lower binding energy) corresponds to a +3 valence state. This outcome suggests the intricate chemical bonding present in $Sr_8Ti_7S_{21}$. Similarly, the sulfur $2p_{3/2}$ XPS spectrum of $Sr_8Ti_7S_{21}$ can be categorized into S-A, S-B, and S-C (Figure S4). The primary contributions, S-A and S-B, align with the sulfide lattice, while S-C can be attributed to sulfone, sulfite, and sulfate species.[16]

The electrical conductivity of $Sr_8Ti_7S_{21}$, measured from a 1 cm-diameter pellet (Figure 1j, see details in the SI), was determined to be 1.5 S/cm at room temperature, exhibiting an increased with temperature, indicative of a highly degenerated semiconductor character. The negative Seebeck coefficient suggests an n-type conductivity, likely dominated by S vacancies.

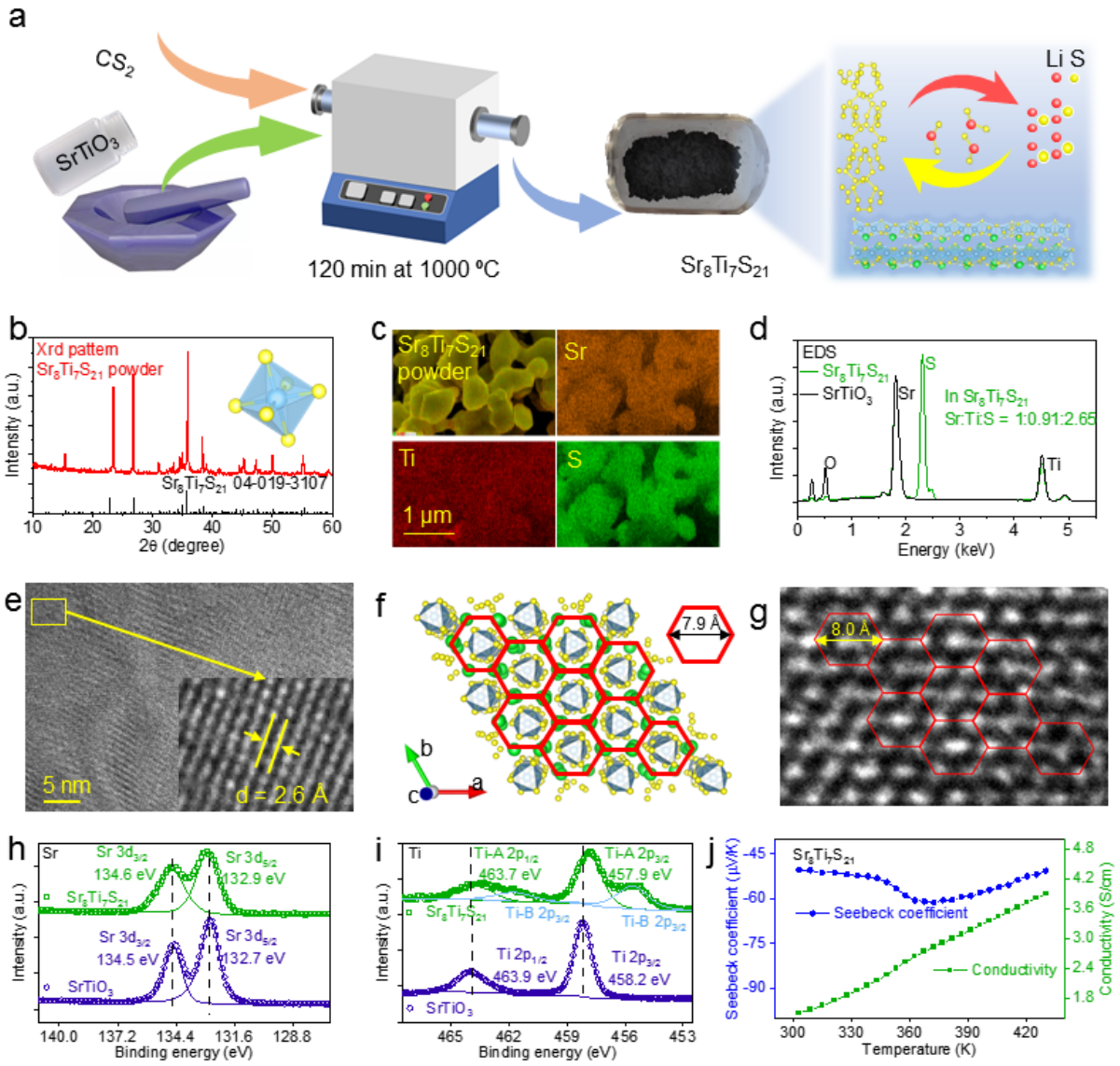

Figure 1. (a) Schematic diagram of the synthesis process used to produce the $Sr_8Ti_7S_{21}$ powder. (b) XRD pattern of the $Sr_8Ti_7S_{21}$ powder including ICDD reference for $Sr_8Ti_7S_{21}$. (c) EDS compositional maps of a $Sr_8Ti_7S_{21}$ powder, showing a uniform elemental distribution. (d) Comparison of the EDS spectra of $SrTiO_3$ and $Sr_8Ti_7S_{21}$, indicating a slight Ti loss during sulfurization. (e) HRTEM images of the perovskite $Sr_8Ti_7S_{21}$. (f) Crystal structure of $Sr_8Ti_7S_{21}$ from the c axis. The green, blue, and yellow balls represent Sr, Ti, and S atoms, respectively. The hexagons formed by Sr are noted in red. (g) HRTEM image of a $Sr_8Ti_7S_{21}$ powder with the hexagons formed by Sr noted in red. (h,i) XPS spectra of Sr, Ti, S elements from $Sr_8Ti_7S_{21}$ powder. (j) Seebeck coefficient and electrical conductivity measured from a $Sr_8Ti_7S_{21}$ pellet.

LiPS adsorption tests were conducted to assess the host material's capability to inhibit LiPS migration in LSBs. To this end, equal amounts of different hosts, $Sr_8Ti_7S_{21}$, and a reference carbon material (Super P), was immersed in a 1×10^{-2} M Li_2S_4 solution. After 12 h, the solution containing $Sr_8Ti_7S_{21}$ exhibited a fading yellowish color, in stark contrast to the solution containing Super P, which retained the dark yellow color characteristic of Li_2S_4 (**Figure 2a**). This observation was further corroborated by the UV-vis spectrum of the solutions in the 400-500 cm^{-1} range.[17] $Sr_8Ti_7S_{21}$ displayed the lowest LiPS-related absorbance peaks, indicating the least amount of LiPS residue in the solution. This underscores the robust LiPS adsorption capability of $Sr_8Ti_7S_{21}$ compared to the conventional carbonaceous support.

The XPS spectra of the samples before and after the adsorption experiment are compared in Figures 2b-d and S5. Following Li_2S_4 adsorption, the Li 1s spectrum shifted towards lower binding energies, indicative of a chemical bond (Li-S) with an electron transfer from $Sr_8Ti_7S_{21}$ perovskites to the Li ions in Li_2S_4 (Figure S5).[18] Figure 2b,c depicts the Sr 3d and Ti 2p XPS spectra of $Sr_8Ti_7S_{21}$ and $Sr_8Ti_7S_{21}$-Li_2S_4. Post interaction with Li_2S_4, the Sr 3d and Ti 2p spectra also shifted to lower binding energies, signifying an electron transfer from Li_2S_4 species to metal ions and confirming the formation of Sr/Ti-S bonds.[19] Additionally, a slight reduction in the relative intensity of the $2p_{3/2}$ peaks was observed, indicating a subtle reduction of this component after Li_2S_4 interaction, further suggesting the formation of Ti-S bonds in the $Sr_8Ti_7S_{21}$-Li_2S_4 composite. Furthermore, as illustrated in Figure 2d, the S 2p spectrum of $Sr_8Ti_7S_{21}$-Li_2S_4 shifted to higher binding energies, indicating a strong interaction between

$Sr_8Ti_7S_{21}$ and polysulfide during the lithium sulfide oxidation process.[19a, 20] In summary, these results affirm a strong interaction between $Sr_8Ti_7S_{21}$ and the LiPSs.

DFT calculations were performed to evaluate the interaction between LiPS and the host materials (Figure 2e-h). According to DFT results, $Sr_8Ti_7S_{21}$ renders a high binding energy (E_b) of -1.37 eV to Li_2S_4. In contrast, the porous carbon used as a reference provides a lower E_b of -0.58 eV. LiPS trapping on $Sr_8Ti_7S_{21}$ is enhanced owing to the high density of lithiophilic/sulfiphilic surface sites. Figures S6 and S7 display the optimized adsorption configuration of LiPS species at six different lithiation stages (Li_2S, Li_2S_2, Li_2S_4, Li_2S_6, Li_2S_8 and S_8) on Super P and perovskites $Sr_8Ti_7S_{21}$. $Sr_8Ti_7S_{21}$ displays potential for Li-S bonds and dual S-Sr/Ti bonds, which endows this material with a strong interaction with LiPS through a multi-bonding effect.

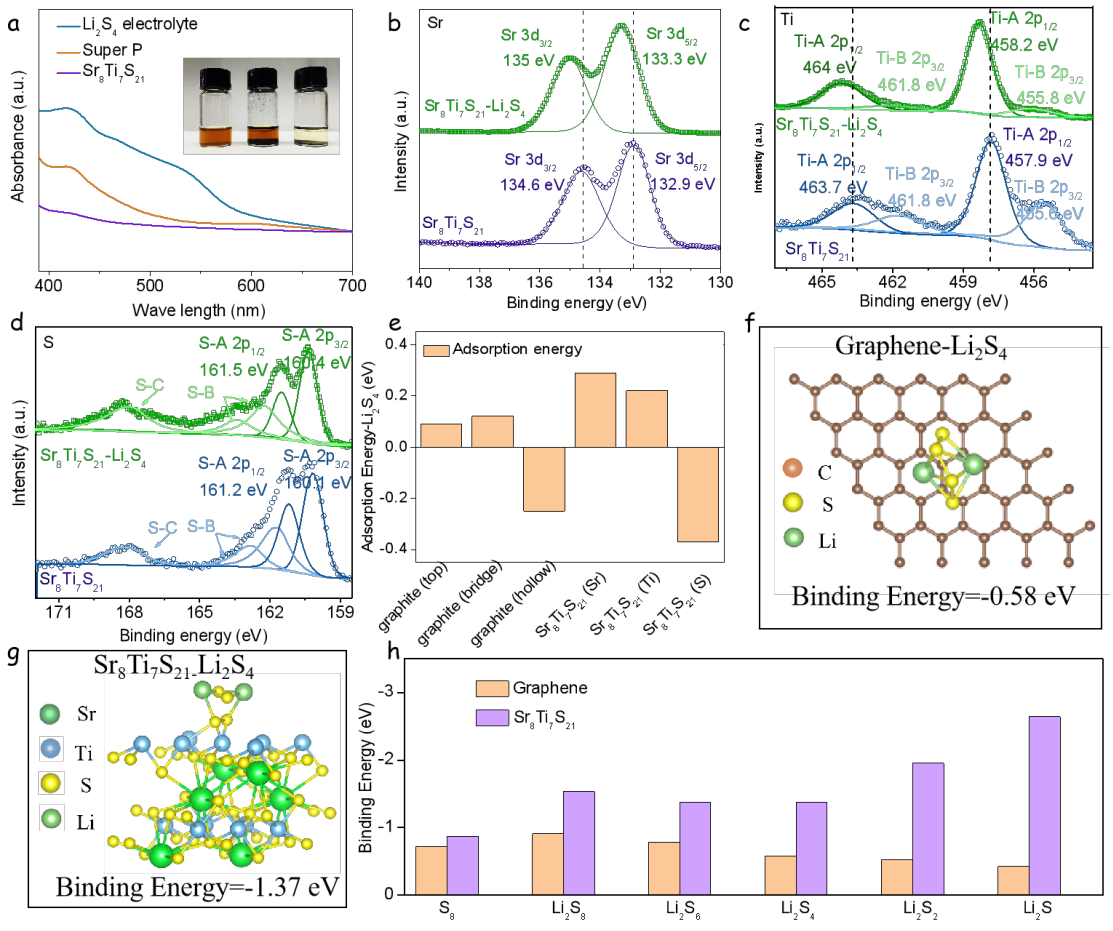

Figure 2. (a) UV-Vis spectra and optical photograph of the flasks containing a Li_2S_4 solution and different adsorbent materials after overnight adsorption. (b) High-resolution Sr 3d and (c) Ti 2p XPS spectra of $Sr_8Ti_7S_{21}$ before and after Li_2S_4 adsorption. (d) S 2p XPS spectra before

and after the interaction of $Sr_8Ti_7S_{21}$ with Li_2S_4. (e) DFT-calculated Li_2S_4 adsorption energy on different surface sites. (f,g) Relaxed Li_2S_4-adsorbed structures on the surface of graphene (f) and $Sr_8Ti_7S_{21}$ (g). (h) Binding energies between LiPS (Li_2S, Li_2S_2, Li_2S_4, Li_2S_6, Li_2S_8 and S_8) and graphene or $Sr_8Ti_7S_{21}$ surfaces.

DFT calculations were also used to determine the perovskite $Sr_8Ti_7S_{21}$ configuration, its band structure, Li-ion diffusivity, and polysulfide conversion activity (**Figure 3**). According to DFT results, $Sr_8Ti_7S_{21}$ showed a low bandgap of 0.47 eV (Figure 3a). The electron localization function (ELF) was used to visualize its electronic structure. Within the ELF, the warmer the color, i.e. values closer to 1, the fewer the delocalized electrons. As expected, we observe a higher density of delocalized electrons around metals, which we hypothesize as the catalytic active sites. The geometrical configurations of the Li-ion diffusion paths and the corresponding energy profiles are displayed in Figure 3b,c. The calculated Li-ion diffusion energy barriers ($E_{barrier}$) for $Sr_8Ti_7S_{21}$ was just 0.36 eV, which is significantly smaller than that of graphene (0.51 eV). The low diffusion barriers allow a faster Li-ion diffusion on the perovskite $Sr_8Ti_7S_{21}$ surfaces. The initial state, transition state, and final state of Li_2S decomposition on graphene and $Sr_8Ti_7S_{21}$ are displayed in Figures 3d,e and S8. The calculated energy barrier of Li_2S decomposition on the surface of the $Sr_8Ti_7S_{21}$ was only 0.55 eV, much lower than on graphene (1.12 eV). This result points to more effective oxidation of Li_2S into LiPS on the $Sr_8Ti_7S_{21}$ surface than on graphene during charging, leading to enhanced redox reversibility between Li_2S and LiPS.[21] Besides, the Gibbs free energies of the main reduction products (S_8, Li_2S_8, Li_2S_6, Li_2S_4, Li_2S_2, and Li_2S) with optimized structures on the surfaces of graphene and perovskites $Sr_8Ti_7S_{21}$ are displayed in Figure 3f. Generally, the largest increase of Gibbs free energy (ΔE) is obtained for the reduction of Li_2S_2 to Li_2S, which is considered the rate-limiting step for the total discharge process in LSBs.[21b, 22] $Sr_8Ti_7S_{21}$ was characterized by a much lower ΔE (0.89 eV) than carbon (1.12 eV), further demonstrating that the reduction of S is more thermodynamically favorable on $Sr_8Ti_7S_{21}$ than on graphene.

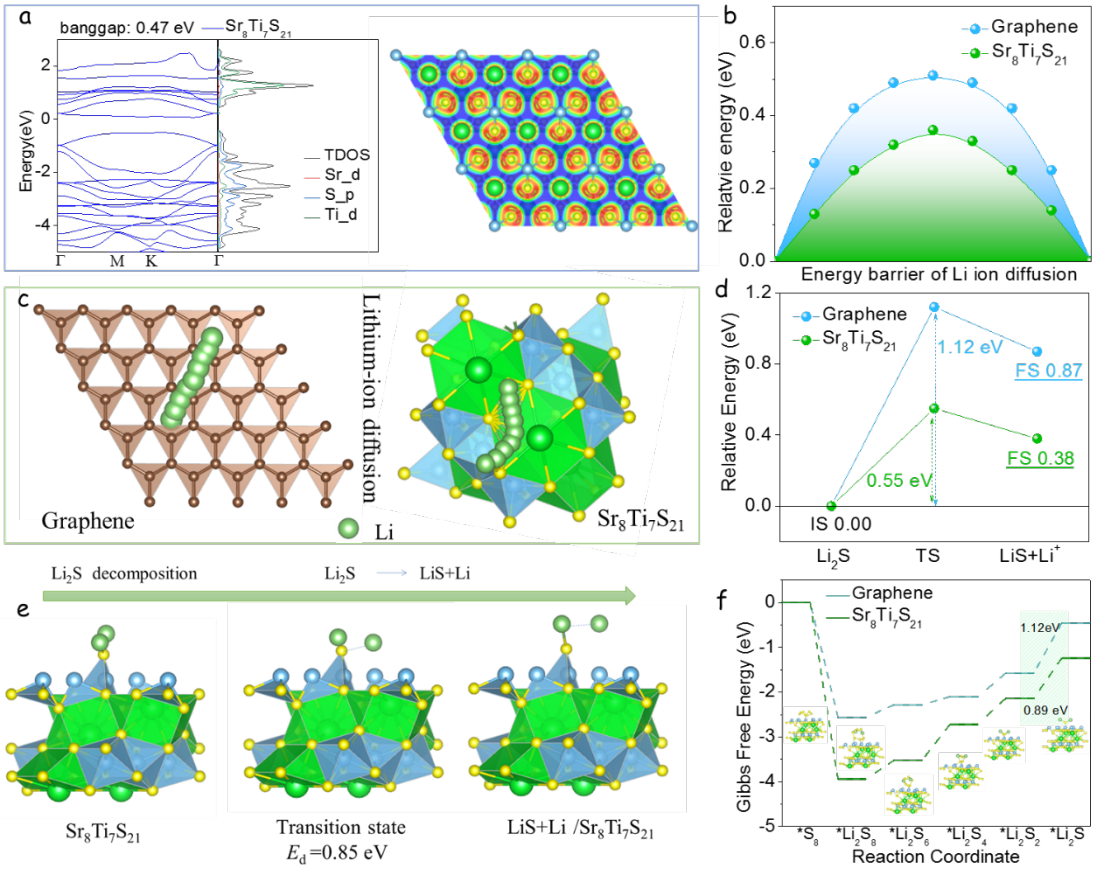

Figure 3. (a) Band structure, density of states, and ELF of $Sr_8Ti_7S_{21}$. (b) Energy barrier of Li-ion diffusion on the surface of graphene and $Sr_8Ti_7S_{21}$. (c) Geometrical configurations of the minimum energy path of Li-ion diffusion on the surface of graphene and $Sr_8Ti_7S_{21}$. (d) Energy barrier profiles of Li_2S decomposition on graphene and $Sr_8Ti_7S_{21}$ along with different reaction coordinates. (e) Initial state, transition state, and final state of Li_2S decomposition on the facet of graphene and $Sr_8Ti_7S_{21}$. (f) Gibbs free energy profiles and adsorption conformation of LiPS species on $Sr_8Ti_7S_{21}$, showing a much lower reaction free energy from Li_2S_2 to Li_2S on $Sr_8Ti_7S_{21}$ than graphene.

To analyze the electrochemical performance of perovskites $Sr_8Ti_7S_{21}$ as a sulfur host in LSBs, sulfur was intermixed with the perovskite $Sr_8Ti_7S_{21}$ sample by a melt-diffusion process. XRD patterns of the obtained S@$Sr_8Ti_7S_{21}$ composite display the presence of crystalline sulfur (JCPDS No. 08-0247, Figure S9).[23] The sulfur content was quantified at 69.8 wt% by thermogravimetric analysis (TGA, Figure S10). In addition, the Brunauer–Emmett–Teller (BET) specific surface area of the material was observed to sharply decrease from 66.8 m^2 g^{-1}

($Sr_8Ti_7S_{21}$) to 11.2 $m^2 g^{-1}$ ($S@Sr_8Ti_7S_{21}$) with the introduction of sulfur, as shown in Figure S11. These results overall verify that a large amount of sulfur was incorporated into the perovskites $Sr_8Ti_7S_{21}$ host.

Li-S coin cells were assembled using a $S@Sr_8Ti_7S_{21}$–based cathode to study the electrocatalytic performance of the electrode materials (see details in the SI). As shown in **Figure 4a**, $S@Sr_8Ti_7S_{21}$ electrodes display two well-defined cathodic peaks associated with the reduction of solid-state S into soluble long-chain LiPS (Li_2S_x, $4 < x < 8$, peak C1) and the subsequent conversion to insoluble Li_2S_2/Li_2S (peak C2).[24] The anodic peak (peak A) corresponds to the reverse oxidation conversion from Li_2S to LiPS and ultimately to S.[24b, 25] $S@Sr_8Ti_7S_{21}$ electrodes exhibit much higher peak currents and cathodic/anodic peaks located at more positive/negative potentials than S@Super P, demonstrating that $Sr_8Ti_7S_{21}$ is an effective catalyst in promoting the polysulfides redox reaction kinetics. To quantify the electrocatalytic activity, we compared the onset potentials at a current density of 10 μA cm^{-2} beyond the baseline current (Figure 4b and Figure S12).[26] Cells based on $S@Sr_8Ti_7S_{21}$ cathodes displayed higher/lower onset potentials for cathodic/anodic peaks, demonstrating faster redox kinetics for the LiPS conversion reaction.

The electrocatalytic activity of $Sr_8Ti_7S_{21}$-based electrodes was further analyzed by cyclic voltammetry (CV) tests at different scan rates from 0.1-0.4 mVs^{-1} (Figure 4c). With an increase in the scan rate, the CV curves indicated that $S@Sr_8Ti_7S_{21}$ cathodes exhibited sharper redox peaks and a smaller overpotential compared with S@Super P cathodes (Figure S13). The CV curves measured from $S@Sr_8Ti_7S_{21}$ cathodes almost overlapped during the first three cycles, indicating good reversibility of the sulfur redox reactions (Figure S14).

The Li^+ ion diffusivity was experimentally determined by measuring CV curves at various scan rates. The cathodic/anodic peak currents showed a linear relationship with the square root of the scanning rates, pointing at a diffusion-limited reaction (Figure 4d-f). Thus, the Randles-Sevcik equation was applied to calculate the Li^+ diffusion coefficient (D_{Li+}) in the process:[27]

$$I_P = (2.69 * 10^5) n^{1.5} A D_{Li+}^{0.5} C_{Li+} v^{0.5} \quad (1)$$

where I_p is the peak current density, n is the number of charges transferred, A is the geometric area of the electrode, C_{Li+} is the concentration of lithium ions in the cathode, and v is the scan

rate. Being n, A, and C_{Li+} constants, the sharper $I_p/v^{0.5}$ slopes, the faster Li^+ diffusion. The S@$Sr_8Ti_7S_{21}$ electrodes exhibited sharper slopes than S@Super P electrodes, thus indicating a higher Li^+ diffusivity during the Li-S redox reaction. Quantitatively, the D_{Li+} calculated from peaks C1, C2, and A were 1.5×10^{-7}, 2.4×10^{-7}, and 5.2×10^{-7} cm^2 s^{-1}, respectively, much higher than the values calculated for S@Super P electrodes (Figure 4g).

Symmetric cells were assembled with Li_2S_6 electrolytes to measure the oxidation-reduction kinetics in the liquid-liquid conversion process. Notably, the perovskite $Sr_8Ti_7S_{21}$ was characterized by redox peaks with a higher redox current response than Super P (Figure 4h), indicating that $Sr_8Ti_7S_{21}$ significantly enhances the kinetics of the liquid-liquid conversion reaction.[28]

The electrode reaction process in the discharge process of LSBs includes two parts: liquid-liquid conversion reaction and liquid-solid conversion reaction. Chronoamperometry was used to investigate the nucleation behavior of lithium sulfide and to characterize the catalytic performance of $Sr_8Ti_7S_{21}$ in the liquid-solid conversion reaction. As shown in Figure 4i, $Sr_8Ti_7S_{21}$ electrodes showed faster responsivity toward Li_2S nucleation and higher capacity of Li_2S precipitation than S@Super P electrodes. The high nucleation capacity of Li_2S proved that $Sr_8Ti_7S_{21}$ effectively catalyzes the liquid-solid conversion kinetics from Li_2S_4 to Li_2S, significantly reducing the energy barrier of the Li_2S nucleation, and enhancing the Li_2S precipitation kinetics.[29]

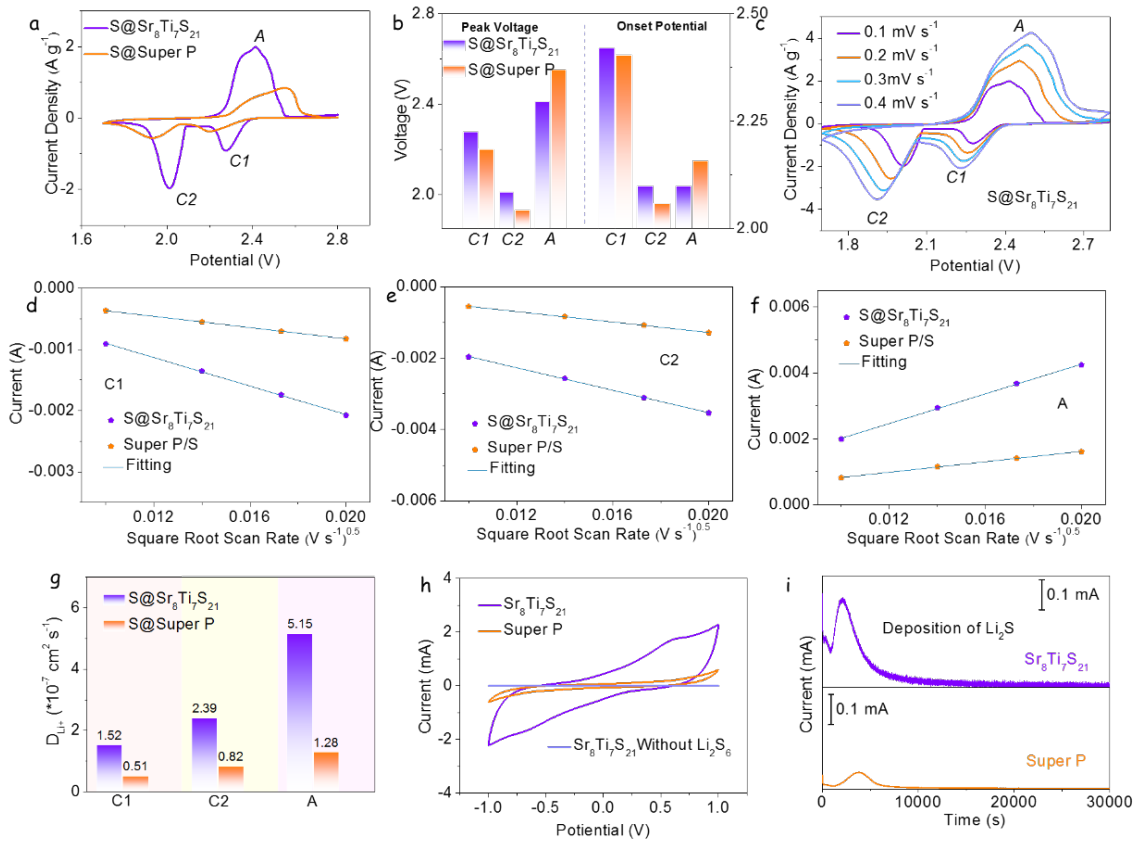

Figure 4. (a) CV profiles of Li–S cells with S@$Sr_8Ti_7S_{21}$ and S@Super P cathodes at 0.1 mV s^{-1} scan rate. (b) Peak potential and onset potential of asymmetric Li–S cells based on the CV curves. (c) CV profiles of the S@$Sr_8Ti_7S_{21}$ electrode with scan rates from 0.1 to 0.4 mV s^{-1}. (d-f) Plots of peak currents versus the square root of the scan rate for the cathodic reduction processes (d,e) and anodic oxidation process (f) in Li–S cells with different electrodes. (g) Li^+ diffusion coefficient calculated from the different CV redox peaks according to the Randles-Sevcik equation. (h) CV curves of symmetric cells at a scan rate of 15 mV s^{-1}. (i) Potentiostatic discharge profile at 2.05 V on different electrodes with Li_2S_8 catholyte for evaluating the nucleation kinetics of Li_2S.

The electrochemical performance was further analyzed through galvanostatic charge/discharge tests. Charge/discharge curves of S@$Sr_8Ti_7S_{21}$ and S@Super P at 0.2 C displayed two discharge plateaus and one charge plateau, consistently with CV results. The voltage gap ΔE between the second reduction and the oxidation plateaus is the polarization potential (**Figure 5a**).[30] S@$Sr_8Ti_7S_{21}$ electrodes were characterized by a significantly lower

polarization potential (ΔE = 150 mV) than S@Super P electrodes (ΔE = 292 mV, Figure 5b), confirming the superior catalytic activity of $Sr_8Ti_7S_{21}$ toward LiPS conversion.

Moreover, discharge curves showed two plateaus, corresponding to the reduction of sulfur to soluble LiPS ($S_8 + 4Li^+ + 4e^- \rightarrow 2Li_2S_4$) and the subsequent conversion to insoluble sulfide ($2Li_2S_4 + 12Li^+ + 12e^- \rightarrow 8Li_2S$).[26b, 31] The associated capacities of each discharge plateau are Q1 and Q2, respectively. The catalytic activity of the host materials toward the LiPS conversion reaction can be also quantified by the ratio Q2/Q1. The higher the Q2/Q1 value, the superior the catalytic ability. S@$Sr_8Ti_7S_{21}$ electrodes showed a high Q2/Q1 ratio at 2.51, well above that of S@Super P (1.17), further proving the superior catalytic properties of perovskite $Sr_8Ti_7S_{21}$ with highly conductive quasi 1D structure towards the LiPS redox reaction.

Electrochemical kinetics were further assessed for the phase conversion between insoluble Li_2S_2/Li_2S and soluble LiPS during the charge/discharge processes.[21b, 32] A voltage dip at the beginning of the initial charging period is associated with the overpotential of the Li_2S oxidation process (Figure S15). S@$Sr_8Ti_7S_{21}$ electrodes were characterized by a lower Li_2S oxidation overpotential compared with S@Super P electrodes, suggesting a promoted Li_2S dissolution.

The galvanostatic charge/discharge voltage profiles of S@$Sr_8Ti_7S_{21}$ electrodes at different current densities from 0.2 C to 4 C are exhibited in Figure 5c. All discharge curves show two well-defined plateaus, even at a higher current density of 4C. In contrast, S@Super P electrodes exhibited a low capacity response and a high polarization potential (Figure S16).

Analyzing the charge/discharge curves of the S@$Sr_8Ti_7S_{21}$ and S@Super P electrodes at various current densities, it is found that the S@$Sr_8Ti_7S_{21}$ electrode has a smaller overpotential and a flatter voltage plateau (Figure 5d).[24b] The overpotentials of the S@$Sr_8Ti_7S_{21}$ electrode at 0.2C, 0.5C, 1C, 2C, and 4C are 150, 205, 251, 362, and 429 mV, confirming that $Sr_8Ti_7S_{21}$ has a strong catalytic conversion ability for LiPS.

Figure 5e shows the rate performance of the cells based on the two electrodes tested, at current rates from 0.2C to 4C. The capacity of the S@$Sr_8Ti_7S_{21}$ electrode was 1315, 1058, 886, 722, and 616 mAh g^{-1} at 0.2C, 0.5C, 1, 2C, and 4 C, respectively, higher than that of S@Super P electrodes, indicating a high utilization of sulfur in the cathode. It is worth mentioning that when the current rate was returned to 0.2C, the average capacity of the cells with the

S@$Sr_8Ti_7S_{21}$ electrode returned to 1180 mAh g^{-1}, pointing toward remarkable reversibility and stability. We hypothesize this high rate performance to be related to the excellent conductivity and the enhanced catalytic activity of the 1D perovskite $Sr_8Ti_7S_{21}$.

EIS analyses were performed to gain additional insight from the enhanced electrochemical performance of S@$Sr_8Ti_7S_{21}$ electrodes. The Nyquist plot obtained from the two electrodes displayed a semicircle in the high-frequency region associated with the charge-transfer resistance (R_{ct}), followed by a linear dependence in the low-frequency region that is related to the diffusion of lithium ions.[21a, 33] Comparing the other two types of electrodes tested, S@$Sr_8Ti_7S_{21}$ electrodes were characterized by a lower R_{ct} (Figure S17).

The cycling stability of the S@$Sr_8Ti_7S_{21}$ and S@Super P electrodes was evaluated by constant current cycling at 0.2C (Figure 5f). The S@$Sr_8Ti_7S_{21}$ electrode displayed an initial discharge capacity of 1266 mAh g^{-1} and maintained a high capacity of 1198 mAh g^{-1} after 100 cycles with only a total of 0.054% capacity loss. In contrast, the discharge capacity of the S@Super P electrodes decayed from 932 to 716 mAh g^{-1} after 100 cycles with a capacity loss of 23.2%. The superior cycling performance of the Li-S cells based on the S@$Sr_8Ti_7S_{21}$ electrodes was associated with the enhanced adsorption and activation of active materials by $Sr_8Ti_7S_{21}$ and the high sulfur utilization rate.

The long-term cycling stability of the $Sr_8Ti_7S_{21}$-based batteries was evaluated at a high current density of 1C (Figure 5g). After 400 cycles, S@$Sr_8Ti_7S_{21}$ electrodes delivered a capacity of 520 mAh g^{-1}, involving a 0.078% average capacity decay per cycle. Meanwhile, a high and steady Coulombic efficiency above 99.2% was consistently measured. Such excellent cycle stability of the S@$Sr_8Ti_7S_{21}$ electrodes was attributed to the high conductivity and superior catalytic activity of $Sr_8Ti_7S_{21}$.

For commercial applications, high energy density LSBs require maximizing the areal sulfur loading and reducing the electrolyte usage. In this direction, we prepared S@$Sr_8Ti_7S_{21}$ electrodes with a sulfur loading of 6.5 mg cm^{-2} and tested them within cells under an electrolyte-to-sulfur (E/S) ratio of 5.8 μL mg^{-1}. When cycled at a 0.2C current rate, the cells based on S@$Sr_8Ti_7S_{21}$ cathodes displayed an initial areal capacity of 6.58 mAh cm^{-2} (Figure 5h), well above that of commercial lithium-ion batteries (4 mAh cm^{-2}).[30b, 34] Besides,

$Sr_8Ti_7S_{21}$-based cells maintained the voltage profile during the 80 cycles, with just a small hysteresis, indicating a minor LiPS migration and stable sulfur electrochemistry (Figure S18).

Overall, S@$Sr_8Ti_7S_{21}$ electrodes were characterized by an excellent electrochemical performance related to the following properties: 1) Perovskite $Sr_8Ti_7S_{21}$ strongly anchors LiPS due to the lithiophilic character of the sulfur sites and the sulfiphilic character of the Sr/Ti metal sites potentially forming multiple bonds to bind LiPS; 2) The quasi-1D geometry of perovskite $Sr_8Ti_7S_{21}$ provide parallel 1D paths for electron conduction and Li^+ diffusion; and 3) The high catalytic activity of perovskite $Sr_8Ti_7S_{21}$ facilitates the kinetics of LiPS redox reactions.

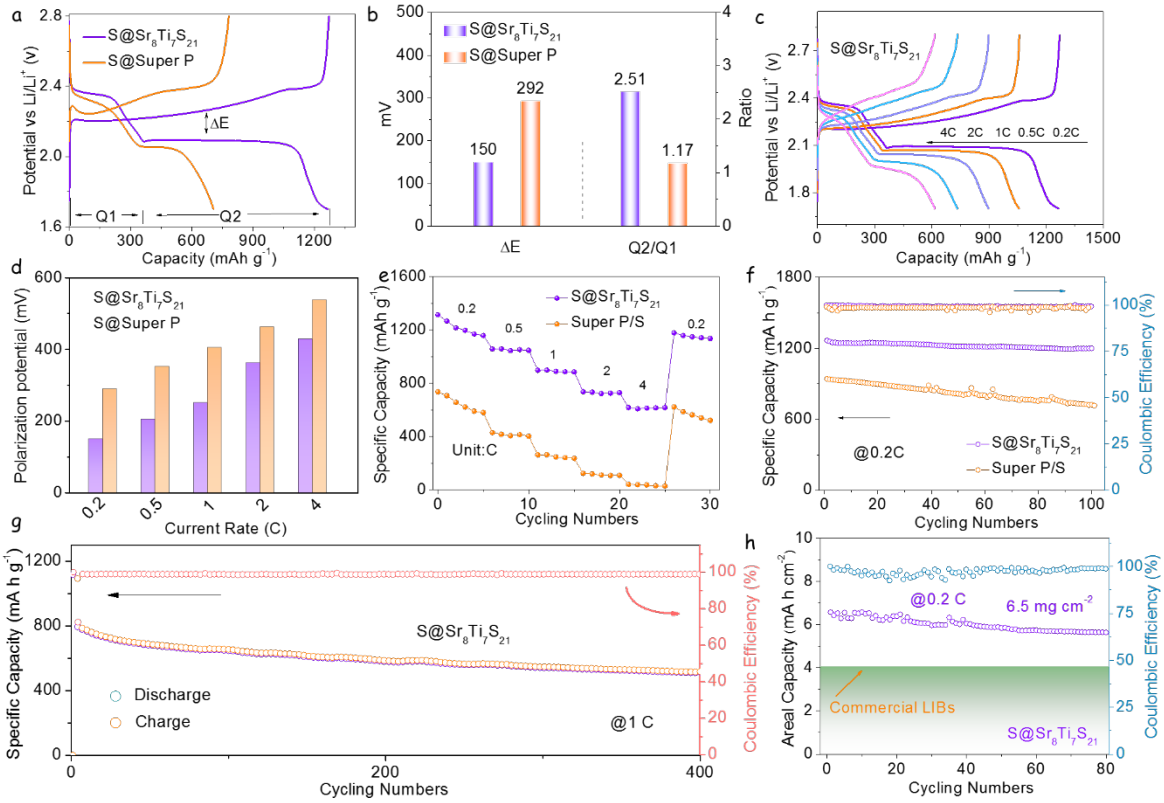

Figure 5. (a) Galvanostatic charge/discharge profiles of S@$Sr_8Ti_7S_{21}$ and S@Super P electrodes at a 0.2C current rate. (b) Values of ΔE and Q2/Q1 resulted from the charge/discharge curves. (c) Galvanostatic charge/discharge profiles at various rates from 0.2C to 4C. (d) Overpotential diagram of the charge/discharge profiles at different rates. (e) Rate capability of different electrodes at various C rates from 0.2C to 4C. (f) Cycling performances and corresponding energy efficiency of different cathodes at 0.2C. (g) Long-term cycling performances of S@$Sr_8Ti_7S_{21}$ electrode at 1C. (h) High-loading cycling performances with a sulfur loading of 6.5 mg cm^{-2} at 0.2C of S@$Sr_8Ti_7S_{21}$ electrode.

3. Conclusion

In summary, we have successfully engineered, characterized, and evaluated a high conductivity 1D $Sr_8Ti_7S_{21}$ perovskite as an efficient sulfur host for LSBs. $Sr_8Ti_7S_{21}$ exhibits multiple lithiophilic/sulfiphilic adsorption sites and exceptional electrocatalytic activities that play a crucial role in regulating polysulfide redox reactions. The multi-bonding effect of LiPS on perovskite $Sr_8Ti_7S_{21}$, facilitated through Li-S and S-Sr/Ti bonds, enhances its LiPS trapping ability, effectively preventing LiPS migration to the anode. This prevents the loss of active material from the cathode, leading to an overall increase of capacity. Additionally, $Sr_8Ti_7S_{21}$ provides multifunctional sites that accelerate the redox conversion of LiPS, reducing the energy barrier of Li_2S deposition/decomposition during discharge/charge processes.

Furthermore, the quasi-1D hexagonal perovskite $Sr_8Ti_7S_{21}$ offers parallel 1D paths for both electron transportation and Li^+ diffusion. Experimental results were substantiated by DFT calculations. Overall, the S@$Sr_8Ti_7S_{21}$ composite demonstrated impressive rate performance, delivering 722 mAh g^{-1} at 2 C, nearly three times larger than carbon-based LSB cathodes). Even at a high sulfur loading of 6.5 mg cm^{-2}, S@$Sr_8Ti_7S_{21}$ cathodes exhibited a remarkable areal capacity of 6.58 mAh cm^{-2}, meeting the requirements of commercial LIBs (4 mAh cm^{-2}). This work provides valuable insights for designing chalcogenide perovskite-based hosts to maximize activity and enhance the performance of LSBs.

Acknowledgements

D. Yang and Y. Han contributed equally to this work. The authors thank the support from the projects ENE2016-77798-C4-3-R and NANOGEN (PID2020-116093RB-C43), funded by MCIN/ AEI/10.13039/501100011033/ and by "ERDF A way of making Europe", by the "European Union". ICN2 acknowledges funding from Generalitat de Catalunya 2021SGR00457. This study is part of the Advanced Materials programme and was supported by MCIN with funding from European Union NextGenerationEU (PRTR-C17.I1) and by Generalitat de Catalunya. ICN2 is supported by the Severo Ochoa program from Spanish MCIN / AEI (Grant No.: CEX2021-001214-S) and is funded by the CERCA Programme / Generalitat

de Catalunya. D. Yang thanks the China Scholarship Council for the scholarship support and the funding from the National Natural Science Foundation of China (NSFC) (Grants No. 22305064). Y. Han thanks the National Natural Science Foundation of China (NSFC) (Grants No. 62104215).

References

[1] a)P. G. Bruce, S. A. Freunberger, L. J. Hardwick, J.-M. Tarascon, *Nat. Mater.* **2012**, 11, 19; b)X. Zhang, T. Yang, Y. Zhang, X. Wang, J. Wang, Y. Li, A. Yu, X. Wang, Z. Chen, *Adv. Mater.* **2023**, 35, 2208470.

[2] G. Zhou, D.-W. Wang, F. Li, P.-X. Hou, L. Yin, C. Liu, G. Q. M. Lu, I. R. Gentle, H.-M. Cheng, *Energy Environ. Sci.* **2012**, 5, 8901.

[3] a)X. Chen, H.-J. Peng, R. Zhang, T.-Z. Hou, J.-Q. Huang, B. Li, Q. Zhang, *ACS Energy Lett.* **2017**, 2, 795; b)Y. Yang, G. Zheng, Y. Cui, *Chem. Soc. Rev.* **2013**, 42, 3018.

[4] J. He, L. Luo, Y. Chen, A. Manthiram, *Adv. Mater.* **2017**, 29, 1702707.

[5] a)Z. Yu, M. Liu, D. Guo, J. Wang, X. Chen, J. Li, H. Jin, Z. Yang, X. a. Chen, S. Wang, *Angew. Chem. Int. Ed.* **2020**, 59, 6406; b)Z. Sun, J. Zhang, L. Yin, G. Hu, R. Fang, H.-M. Cheng, F. Li, *Nat. Commun.* **2017**, 8, 14627.

[6] a)X. Liu, J. Q. Huang, Q. Zhang, L. Mai, *Adv. Mater.* **2017**, 29, 1601759; b)J. Zhang, Z. Li, Y. Chen, S. Gao, X. W. Lou, *Angew. Chem. Int. Ed.* **2018**, 57, 10944; c)D. Yang, M. Li, X. Zheng, X. Han, C. Zhang, J. Jacas Biendicho, J. Llorca, J. Wang, H. Hao, J. Li, *ACS nano* **2022**, 16, 11102.

[7] a)W. Hua, H. Li, C. Pei, J. Xia, Y. Sun, C. Zhang, W. Lv, Y. Tao, Y. Jiao, B. Zhang, *Adv. Mater.* **2021**, 33, 2101006; b)Y. Zhong, Q. Wang, S.-M. Bak, S. Hwang, Y. Du, H. Wang, *J. Am. Chem. Soc.* **2023**, 145, 7390.

[8] Y. Liang, Y. Zhang, J. Xu, J. Ma, H. Jiang, X. Li, B. Zhang, X. Chen, Y. Tian, Y. Han, Z. Shi, *Nano Res.* **2022**, 16, 7867.

[9] a)J. Xu, Y. Fan, W. Tian, L. Ye, Y. Zhang, Y. Tian, Y. Han, Z. Shi, *J. Solid State Chem.* **2022**, 307, 122872; b)Y. Nishigaki, T. Nagai, M. Nishiwaki, T. Aizawa, M. Kozawa, K. Hanzawa, Y. Kato, H. Sai, H. Hiramatsu, H. Hosono, H. Fujiwara, *Solar RRL* **2020**, 4, 1900555.

[10] X. Wu, W. Gao, J. Chai, C. Ming, M. Chen, H. Zeng, P. Zhang, S. Zhang, Y.-Y. Sun, *Sci. China Mater.* **2021**, 64, 2976.

[11] Y. Han, J. Xu, Y. Liang, X. Chen, M. Jia, J. Zhang, L. Lian, Y. Liu, X. Li, Z. Shi, *Chem. Eng. J.* **2023**, 473, 145351.

[12] S. Niu, G. Joe, H. Zhao, Y. Zhou, T. Orvis, H. Huyan, J. Salman, K. Mahalingam, B. Urwin, J. Wu, Y. Liu, T. E. Tiwald, S. B. Cronin, B. M. Howe, M. Mecklenburg, R. Haiges, D. J. Singh, H. Wang, M. A. Kats, J. Ravichandran, *Nat. Photonics* **2018**, 12, 392.

[13] J. H. Al Shuhaib, J. F. Fernández, J. Bodega, J. R. Ares, I. J. Ferrer, F. Leardini, *Mater. Res. Bull.* **2023**, 112405.

[14] J. Wu, X. Cong, S. Niu, F. Liu, H. Zhao, Z. Du, J. Ravichandran, P. H. Tan, H. Wang, *Adv. Mater.* **2019**, 31, 1902118.

[15] W. M. Haynes, *CRC Handbook of Chemistry and Physics*, **2017**.

[16] J. Chastain, R. C. King Jr, *Handbook of X-ray photoelectron spectroscopy*, Vol. 40, **1992**.

[17] a)W. Chen, T. Lei, W. Lv, Y. Hu, Y. Yan, Y. Jiao, W. He, Z. Li, C. Yan, J. Xiong, *Adv. Mater.* **2018**, 30, 1804084; b)C. Zhang, B. Fei, D. Yang, H. Zhan, J. Wang, J. Diao, J. Li, G. Henkelman, D. Cai, J. J. Biendicho, *Adv. Funct. Mater.* **2022**, 32, 2201322.

[18] J. Xu, W. Zhang, H. Fan, F. Cheng, D. Su, G. Wang, *Nano Energy* **2018**, 51, 73.

[19] a)R. Dai, Y. Zhang, J. Fan, Q. Xu, Y. Min, *ACS Sustain. Chem. Eng.* **2020**, 8, 18636; b)L. Kong, X. Chen, B. Q. Li, H. J. Peng, J. Q. Huang, J. Xie, Q. Zhang, *Adv. Mater.* **2018**, 30, 1705219.
[20] P. Chen, T. Wang, F. Tang, G. Chen, C. Wang, *Chem. Eng. J.* **2022**, 446, 136990.
[21] a)D. Yang, Z. Liang, P. Tang, C. Zhang, M. Tang, Q. Li, J. J. Biendicho, J. Li, M. Heggen, R. E. Dunin‐Borkowski, *Adv. Mater.* **2022**, 34, 2108835; b)Z. Du, X. Chen, W. Hu, C. Chuang, S. Xie, A. Hu, W. Yan, X. Kong, X. Wu, H. Ji, *J. Am. Chem. Soc.* **2019**, 141, 3977.
[22] Z. Liang, D. Yang, P. Tang, C. Zhang, J. Jacas Biendicho, Y. Zhang, J. Llorca, X. Wang, J. Li, M. Heggen, *Adv. Energy Mater.* **2021**, 11, 2003507.
[23] C. Dai, L. Hu, M.-Q. Wang, Y. Chen, J. Han, J. Jiang, Y. Zhang, B. Shen, Y. Niu, S.-J. Bao, *Energy. Stor. Mater.* **2017**, 8, 202.
[24] a)Y. Ding, Q. Cheng, J. Wu, T. Yan, Z. Shi, M. Wang, D. Yang, P. Wang, L. Zhang, J. Sun, *Adv. Mater.* **2022**, 34, 2202256; b)D. Yang, C. Zhang, J. J. Biendicho, X. Han, Z. Liang, R. Du, M. Li, J. Li, J. Arbiol, J. Llorca, *ACS nano* **2020**, 14, 15492.
[25] Y. Song, L. Zou, C. Wei, Y. Zhou, Y. Hu, *Carbon Energy* **2023**, 5, e286.
[26] a)Z. Yuan, H.-J. Peng, T.-Z. Hou, J.-Q. Huang, C.-M. Chen, D.-W. Wang, X.-B. Cheng, F. Wei, Q. Zhang, *Nano Lett.* **2016**, 16, 519; b)D. Yang, Z. Liang, C. Zhang, J. J. Biendicho, M. Botifoll, M. C. Spadaro, Q. Chen, M. Li, A. Ramon, A. O. Moghaddam, *Adv. Energy Mater.* **2021**, 11, 2101250.
[27] a)X. Sun, D. Tian, X. Song, B. Jiang, C. Zhao, Y. Zhang, L. Yang, L. Fan, X. Yin, N. Zhang, *Nano Energy* **2022**, 95, 106979; b)G. Liu, W. Wang, P. Zeng, C. Yuan, L. Wang, H. Li, H. Zhang, X. Sun, K. Dai, J. Mao, *Nano Lett.* **2022**, 22, 6366; c)N. Shi, B. Xi, J. Liu, Z. Zhang, N. Song, W. Chen, J. Feng, S. Xiong, *Adv. Funct. Mater.* **2022**, 32, 2111586.
[28] a)Y. Liu, M. Zhao, L. P. Hou, Z. Li, C. X. Bi, Z. X. Chen, Q. Cheng, X. Q. Zhang, B. Q. Li, S. Kaskel, *Angew. Chem. Int. Ed.* **2023**, 62, e202303363; b)H. Lin, L. Yang, X. Jiang, G. Li, T. Zhang, Q. Yao, G. W. Zheng, J. Y. Lee, *Energy Environ. Sci.* **2017**, 10, 1476; c)C. Ma, Y. Zhang, Y. Feng, N. Wang, L. Zhou, C. Liang, L. Chen, Y. Lai, X. Ji, C. Yan, *Adv. Mater.* **2021**, 33, 2100171.
[29] a)S. Wang, F. Huang, X. Li, W. Li, Y. Chen, X. Tang, S. Jiao, R. Cao, *ACS Appl. Mater. Interfaces* **2022**, 14, 4204; b)F. Y. Fan, W. C. Carter, Y. M. Chiang, *Adv. Mater.* **2015**, 27, 5203.
[30] a)H. Li, L. Fei, R. Zhang, S. Yu, Y. Zhang, L. Shu, Y. Li, Y. Wang, *J. Energy Chem.* **2020**, 49, 339; b)M. Li, D. Yang, J. J. Biendicho, X. Han, C. Zhang, K. Liu, J. Diao, J. Li, J. Wang, M. Heggen, *Adv. Funct. Mater.* **2022**, 32, 2200529.
[31] M. Du, P. Geng, C. Pei, X. Jiang, Y. Shan, W. Hu, L. Ni, H. Pang, *Angew. Chem. Int. Ed.* **2022**, 134, e202209350.
[32] C. Zhang, R. Du, J. J. Biendicho, M. Yi, K. Xiao, D. Yang, T. Zhang, X. Wang, J. Arbiol, J. Llorca, *Adv. Energy Mater.* **2021**, 11, 2100432.
[33] Y. Qiu, L. Fan, M. Wang, X. Yin, X. Wu, X. Sun, D. Tian, B. Guan, D. Tang, N. Zhang, *ACS nano* **2020**, 14, 16105.
[34] Y. Tian, G. Li, Y. Zhang, D. Luo, X. Wang, Y. Zhao, H. Liu, P. Ji, X. Du, J. Li, *Adv. Mater.* **2020**, 32, 1904876.

Rationally designed multifunctional polysulfide mediators based on a quasi-1D hexagonal chalcogenide perovskite, $Sr_8Ti_7S_{21}$, are demonstrated as excellent cathode materials in lithium-sulfur batteries (LSBs), realizing the adsorption-catalysis-conversion of polysulfides, and thus batteries with exceptional lifespan are delivered.

Keyword: Lithium-sulfur battery

Dawei Yang+,*, Yanbing Han+, Mengyao Li, Canhuang Li, Wei Bi, Qianhong Gong, Jinglu Zhang, Han Gao, Jordi Arbiol, Zhifeng Shi*, Guangmin Zhou*, Andreu Cabot*

Highly Conductive Quasi-1D Hexagonal Chalcogenide Perovskite $Sr_8Ti_7S_{21}$ with Efficient Polysulfide Regulation in Lithium-Sulfur Batteries

ToC figure: